Atomic-resolution chemical mapping of ordered precipitates in Al alloys using energy-dispersive X-ray spectroscopy

Sigurd Wenner*[a], Lewys Jones[b], Calin D. Marioara[c], Randi Holmestad[a]

[a] Department of Physics, NTNU – Trondheim, NO-7491 Trondheim, Norway

[b] Department of Materials, University of Oxford, Parks Road, OX1 3PH Oxford, UK

[c] Materials and Chemistry, SINTEF, NO-7491 Trondheim, Norway

Abstract

Scanning transmission electron microscopy (STEM) coupled with energy-dispersive X-ray spectroscopy (EDS) is a common technique for chemical mapping in thin samples. Obtaining high-resolution elemental maps in the STEM is jointly dependent on stepping the sharply focused electron probe in a precise raster, on collecting a significant number of characteristic X-rays over time, and on avoiding damage to the sample. In this work, 80 kV aberration-corrected STEM-EDS mapping was performed on ordered precipitates in aluminium alloys. Probe and sample instability problems are handled by acquiring series of annular dark-field (ADF) images and simultaneous EDS volumes, which are aligned and non-rigidly registered after acquisition. The summed EDS volumes yield elemental maps of Al, Mg, Si, and Cu, with sufficient resolution and signal-to-noise ratio to determine the elemental species of each atomic column in a periodic structure, and in some cases the species of single atomic columns. Within the uncertainty of the technique, S and β'' phases were found to have pure elemental atomic columns with compositions Al_2CuMg and $Al_2Mg_5Si_4$, respectively. The Q' phase showed some variation in chemistry across a single precipitate, although the majority of unit cells had a composition $Al_6Mg_6Si_{7.2}Cu_2$.

Keywords

scanning transmission electron microscopy, energy-dispersive X-ray spectroscopy, aluminium alloys, precipitation.

1. Introduction

Atomic-resolution spectroscopy in the (scanning) transmission electron microscope (STEM) is becoming increasingly commonplace. Due to fast acquisition and information-rich spectra, electron energy loss spectroscopy (EELS) is the dominant technique for many materials. It can give information on thickness, oxidation state, chemical bonding, magnetic and optic properties in addition to elemental presence. Conversely, X-ray energy-dispersive spectroscopy (EDS) only measures the elemental composition, and requires exposing a specimen to a vast amount of electrons in order to produce enough signal to extract atomic-resolution information. Nevertheless, some excellent high-resolution EDS maps of small areas have been created, of materials such as oxides (Feng et al., 2016; Dycus et al., 2016; D'Alfonso et al. 2010), semiconductors (Chu et al., 2010; Klenov and Zide, 2011) and magnetic alloys (Lu et al., 2014a). STEM-EELS is the ideal technique only for an ideal specimen; that is a thin, non-contaminating specimen with no carbon or SiN supports (as these elements would

give huge background signals that complicate spectrum analysis). For many samples technologically relevant to the materials scientist STEM-EDS is often more applicable because of these advantages:

- Thicker specimens are manageable as long as electron beam broadening and de-channeling is not too severe. Spatial resolution is typically better than with EELS, as very localized, high-energy peaks are available for mapping (Pennycook, 2012; Allen et al., 2003; Allen et al., 2015).
- Some carbon contamination can be tolerated, where it would completely devastate a high-loss EELS spectrum.
- Overlap between different elemental X-ray peaks is rare, and even in case of overlap the peaks can be deconvoluted due to their simple Gaussian shape.
- Modern silicon drift detectors (SDD) have a negligible and Poisson-distributed dark noise, which means that each elemental peak can be straightforwardly integrated but also summed across multiple spectra, with increasing signal-to-noise ratios for longer acquisitions.
- Any dwell time can be used with STEM, while with EELS some time is used for spectrum readout, preventing fast multi-frame scanning.

For a metallic alloy specimen, which has no interesting electronic properties, and is often limited by thickness and carbon contamination, EDS is therefore the technique most likely to produce useful results. On a microscope equipped with a probe Cs aberration corrector, the points above should make atomically resolved STEM-EDS maps readily obtainable. However, a key problem remains – accumulating enough signal (counts) to yield an unambiguous high-resolution EDS map. Importantly, the count rate is influenced by shadowing of X-ray photons by the specimen holder and the specimen itself, which means that careful preparation is required to optimize the specimen crystallography and geometry. While acquiring an EDS map, a specimen may exhibit both lateral and focal drift, electron lenses may drift from their optimal configurations, and environmental factors may cause distortions in the scanned dataset. Existing multi-frame acquisition approaches with automated lateral-drift correction *between* frames can only partially correct for stage shifts. Environmental distortions, present in all but the most extremely stable microscopes reside *within* each frame, greatly limit the spatial resolution after summing frames together. In the presence of focal drift during the length of the acquisition, the resolution can be degraded even further.

An alternative experimental method, which we apply in this paper, is primarily limited by the sensitivity of the specimen to electron irradiation. Multiple annular dark-field (ADF) STEM images are acquired in series and alongside each its simultaneous EDS volume. The data acquisition can be run continuously, or if necessary, small corrections of stage position, focus and probe astigmatism are made between frames. Using the ADF frames to identify lateral offsets, both small mis-registrations between frames, and non-linear scan distortions within frames, are corrected in post-processing. The probe offsets from the ADF images are used to correct the corresponding EDS volumes, before summing spectral volumes together (Yankovich et al., 2016).

In the special case of ordered structures, the resulting maps may also be averaged over several unit cells, exploiting translational periodicity (and rotational symmetry) to further improve the signal-to-noise ratio (Jeong and Mkhoyan, 2016). In this work, such symmetry averaging is shown to create atomic-resolution EDS maps of nanometer-sized precipitate structures in aluminium alloys. This is a great advancement from composition measurements utilizing lower-magnification EDS mapping or atom-probe tomography (Marlaud et al., 2010; Li et al., 2014), where the atomic structure cannot be resolved. With most atomically resolved spectroscopy being demonstrated on highly stable model systems such as $SrTiO_3$, an application to engineering alloys used in bikes, cars and airplanes should be of broader interest to materials scientists.

Many precipitate structures can be solved by ADF imaging alone: For the S phase in Al–Cu–Mg alloys, at least three candidate structures were considered (Perlitz and Westgren, 1943; Mondolfo, 1976; Kilaas and Radmilovic, 2001), all with composition Al_2MgCu, until one could directly observe the atomic columns with atomic number contrast and identify the Perlitz–Westgren model as correct (Liu et al., 2001). Other structures are still disputed after aberration-corrected ADF imaging due to a content of elements with similar atomic numbers: The β'' phase in Al–Mg–Si alloys was first well established as Mg_5Si_6 (Zandbergen et al., 1997; Chen et al., 2006), then proposed as both $Al_2Mg_5Si_4$ (Hasting et al., 2009) and $Al_3Mg_4Si_4$ (Ninive et al., 2014). The Q' phase in Al–Mg–Si–Cu alloys has been suggested as $Al_3Mg_9Si_7Cu_2$ on the basis of density functional theory calculations (Wolverton, 2001), with no decisive experimental evidence. Our obtained chemical maps indisputably determine the composition of all three phases, concluding several long-standing scientific discussions.

2. Methodology

ADF and EDS data were obtained using a JEOL ARM-200CF double-corrected cold field emission gun microscope. The acceleration voltage was set to 80 kV to minimize electron beam damage during the prolonged scans. The probe current was measured at 155 pA (85 pA for Al–Mg–Si). The beam convergence angle was 34 mrad and the inner and outer collection angles of the ADF detector were 35 and 149 mrad, respectively (to maximize the signal for quick refocusing). X-ray spectra were acquired using a Centurio SDD detector with collection solid angle 0.98 sr and elevation angle 24.3°. The dispersion was set to 10 eV per channel.

Scans with 256x256 pixels were acquired with a 500 µs dwell time, giving a frame time of 33 seconds. The pixel size was 30 pm. With a typical image series of 50 frames, including the time required to correct stage position, focus and astigmatism, one hour was spent scanning each specimen. This exposes the scanned area to a total dose of 7800 pC/nm^2 or 4.85×10^{10} $electrons/nm^2$. Line synchronization was avoided to ensure the scan distortions were uncorrelated between image frames.

To maximize the precision of the image shift and scan distortion measurement, a radial Wiener filter and background trend subtraction were applied to compensate for electronic noise and carbon deposition, respectively. Digital super-resolution via pixel up-sampling (2x) was applied to exploit the subpixel precision acquired in interpolation. Images and their corresponding EDS volumes were then aligned, non-rigidly registered and summed up using the Smart Align software (Jones et al., 2015). Additional periodic averaging was done spatially over repeating formula units in the projected image (1 or ½ unit cell), along with rotational averaging when appropriate. Such averaging is highly useful when symmetries are present, but cannot be applied to disordered precipitates, which are important in many Al-based alloy systems (Bjørge et al., 2012; Marioara et al., 2013; Ehlers et al., 2014). To produce chemical maps from the volumes, Kα elemental peaks in the X-ray spectrum were integrated out to the full width at one-third maximum (FWTM), since it includes most of the counts in a peak and is suitable for thin specimens producing little bremsstrahlung (Williams and Carter, 2009).This gives an integration range width of 90–110 eV for Mg, Al and Si, and 190–200 eV for Cu.

In order to understand the change in spectrum image quality with prolonged exposures, the signal-to-background ratio (SBR) and signal-to-noise ratio (SNR) of an elemental map series were quantified. Gaussian functions with centers at the atomic column positions were first least-squares fitted to the summed Cu-Kα map to determine the Gaussian width. Next, each map in the series was fitted with only Gaussian height and constant background level as the two free parameters. The ratio between these quantities defines the SBR: the peak intensity of atomic columns divided by the intensity in-between columns. This is sometimes used as a measure of the contrast in an atomic-resolution image (Dycus et al., 2016). The residual (error) of the fit was used as the noise. The SNR was defined as the

height of the Gaussians (approximately equal to the signal modulation (Lu et al., 2016)) divided by the RMS of the noise. Lu et al. used SNR > 3 as a criterion for atomic column visibility in EDS maps (Lu et al., 2014b).

For a qualitative comparison of EDS and EELS elemental maps, a single-scan EELS volume was acquired from the Al–Mg–Si alloy, yielding a similar SNR as the EDS maps. A dwell time of 10 ms and pixel size of 38 pm were used, and the electron beam parameters were the same as in the STEM–EDS acquisitions. The inner and outer collection angles of the ADF detector were 67 and 155 mrad, respectively. A GIF Quantum spectrometer was used, with a collection angle of 67 mrad, 0.4 eV dispersion and 2048 channels with 4x spectrum binning. Power-law background subtraction and least-squares fitting of K-shell core loss edges were done to construct elemental maps.

The imaged precipitates are of common phases from three industrially relevant Al alloys, nominally Al–Mg–Cu, Al–Mg–Si and Al–Mg–Si–Cu. The first belongs to the 2*xxx* class while the last two are 6*xxx* alloys. Both are classes of age hardenable, medium to high-strength alloys, primarily used for structural parts in automobiles and airplanes. The alloy compositions are given in Table 1, and the details on processing and heat treatment can be found in the Supplementary material. The TEM specimens were prepared by electropolishing. Al grains in the <001> orientation were used, with small stage tilts (0–10°) towards the EDS detector to minimize shadowing effects. Defect-free crystalline precipitates that span through the whole thickness of the TEM specimen were chosen. The scanned areas are estimated to be about 30–40 nm thick based on the EDS count rate, projected density of precipitates and ADF image quality. The precipitate phases were identified based on their crystal structures as reported in the literature (Perlitz and Westgren, 1943; Zandbergen et al., 1997; Arnberg and Aurivillius, 1980). The phases are metastable, i.e. only able to exist when encompassed by the Al matrix. In the TEM specimens, the precipitates are in contact with vacuum (or a surface oxide layer), and are therefore prone to structural change, amorphization or sputtering induced by the electron beam.

TABLE 1: Composition of the three alloys used for this study (mass %).

Alloy	Al	Mg	Si	Cu	Zn	Mn	Fe
Al–Mg–Cu	95.25	1.00		2.00	1.00	0.55	0.20
Al–Mg–Si	98.95	0.37	0.45			0.03	0.20
Al–Mg–Si–Cu	97.26	0.65	0.93	0.40		0.56	0.20

3. Results

Figure 1 shows highlighted features from the acquisition series from an S precipitate in the Al–Mg–Cu alloy. In the summed EDS map in Figure 1(e), the atomic lattice is clearly visible, with 3900 Cu-Kα counts per nm^2. The signal required for obtaining atomic resolution information is much lower than this (Lu et al., 2016). Even the single-frame Cu-Kα image in Figure 1(c), with 88 counts per nm^2, can be used to extract atomic spacing information, e.g. by using its autocorrelation function (Mørtsell et al., 2016), which is shown in the corner of the map. For the three Kα peaks of interest (Al, Mg and Cu), the total number of counts in the aligned images is 350 000. The area of interest was exposed to a total of about 3.4×10^{12} electrons, which gives a net probability of 1 in 10 million that an electron generates a useful X-ray photon which is detected. This highlights the key challenge in recording high-SNR EDX maps without causing excess sample damage.

The Al–Mg–Cu alloy also contains 0.4 at.% Zn. With this overall alloy composition, Zn has been shown to be present in the S phase at a level of about 3 at.% (Wenner et al., 2016). A summed Zn map is

shown in Figure 1(f). The Cu-Zn cross-correlation function reveals a periodicity in the b_S direction, which means that Zn atoms occupy a specific atomic site in the structure. Looking ahead at the atomic structure of the S phase in Figure 3, the cross-correlation is negative (see the inset profile) where we expect Mg columns. This means that Zn atoms are present in-between Mg columns, but whether they occupy Al sites, Cu sites or both, cannot be concluded solely on the basis of this dataset. Periodic averaging does not shed more light on this issue.

In the 59 minutes of electron irradiation between frame 1 and 50, an unavoidable amount of carbon contamination has built up. In Figure 2(a), we show a plot of the total characteristic X-ray counts as a function of time. Carbon contamination has a surprisingly abrupt onset, and saturates after a long time. The Cu and Mg signals decrease slowly with time, which could be caused by sputtering of the precipitate, or reabsorption effects in the deposited carbon. The Gaussian fit to the atomic-columns in the summed Cu map in Figure 1(e) gave a full width at half maximum of 229 pm. In Figure 2(b), the SBR of each Cu-Kα frame is plotted. Because of the intrinsically poor SNR in single frames, the measurement error of the SBR is very high. The SBR of the summed map decreases slightly throughout the acquisition and becomes 0.49 after including 50 frames. The single-frame SNR in Figure 2(c) also decreases slowly. The SNR of the cumulatively summed elemental map however, is found to increase proportionally to the square root of the number of included frames for the first 20 frames. After this the trend falls slightly short of the square root curve, again likely due to carbon contamination issues. It reaches a value of 1.18 when all 50 frames are summed. For comparison, the Mg-Kα image summed over 50 frames has a Gaussian full width at half maximum of 226 pm, SBR = 0.43 and SNR = 0.82.

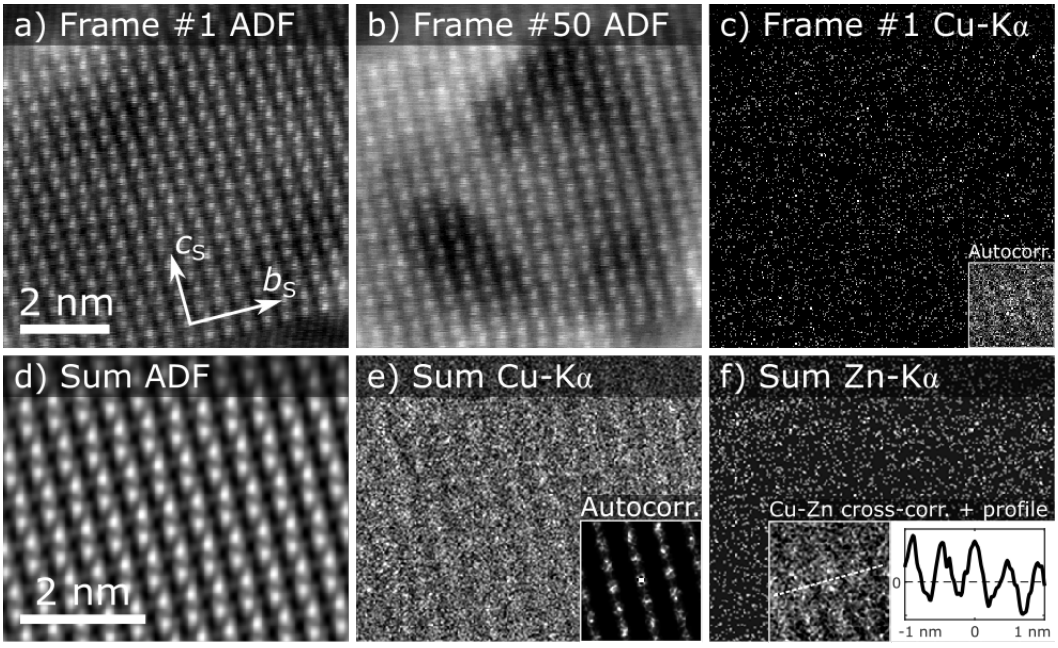

Figure 1: Analysis of frame-wise EDS map acquisitions of an S precipitate in the Al–Mg–Cu alloy. (a,b) The first and last ADF frames. (c) The integrated Cu-Kα image from the first frame. Inset: Cu-Cu autocorrelation function of the image. (d–f) Aligned and summed ADF, Cu-Kα and Zn-Kα images from all 50 frames, respectively. Insets: (e) Cu-Cu autocorrelation function, (f) Cu-Zn cross-correlation function, with integrated profile in the b_S direction.

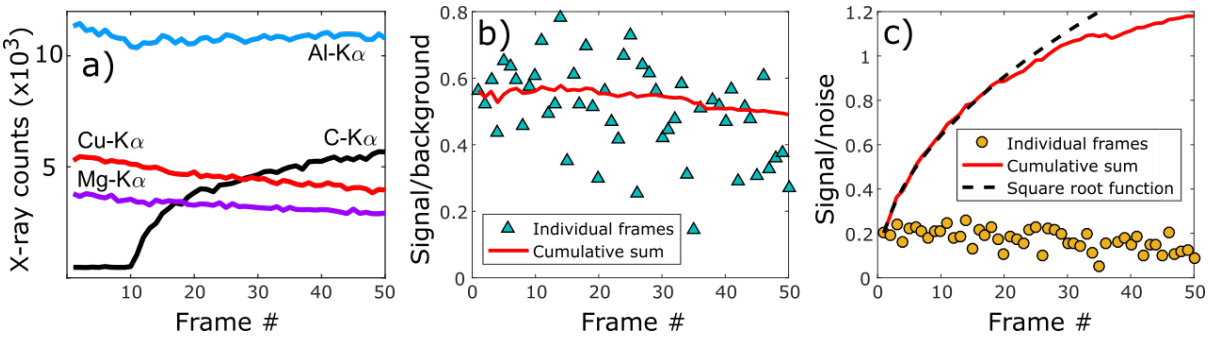

Figure 2: (Color online) (a) The evolution of the integrated intensity in the relevant elemental peaks during the acquisition. (b,c) The SBR and SNR of individual Cu-Kα map frames (and the cumulative sum of frames), as defined in section 2. The dashed line in (c) is the initial SNR value multiplied by the square root of the number of frames.

Symmetry-averaged scans from three types of precipitates in the Al–Mg(–Si)(–Cu) alloys are shown in Figure 3. The original summed EDS images and summed spectra are shown in the Supplementary material. In all these scans, the beam direction is along $<001>_{Al}$, which is the main coherency direction (and direction of precipitate growth during heat treatment) of the three phases. Periodically averaged EELS maps of the β'' phase were also generated. This data comes from a single-frame acquisition, so a slight distortion is present due to stage drift. Although a lower dose (about 1/10) is required to obtain the same quality Al and Mg maps compared with EDS, there is negligible visibility of atomic columns in the Si map. The 2D projected atomic models in the last row in Figure 3 are created by matching atomic positions in the ADF image with an intensity peak in the elemental maps. The repeat distance parallel to the electron beam is a_{Al} = 405 pm for all columns (with one exception in Q', as we will see in section 4), and filled/non-filled circles represent atoms that differ in height by $a_{Al}/2$. It should be noted that symmetry-averaging of inherently noisy data creates some artifacts seen as periodic features in the maps. Any features smaller than the atomic columns do not represent physical information.

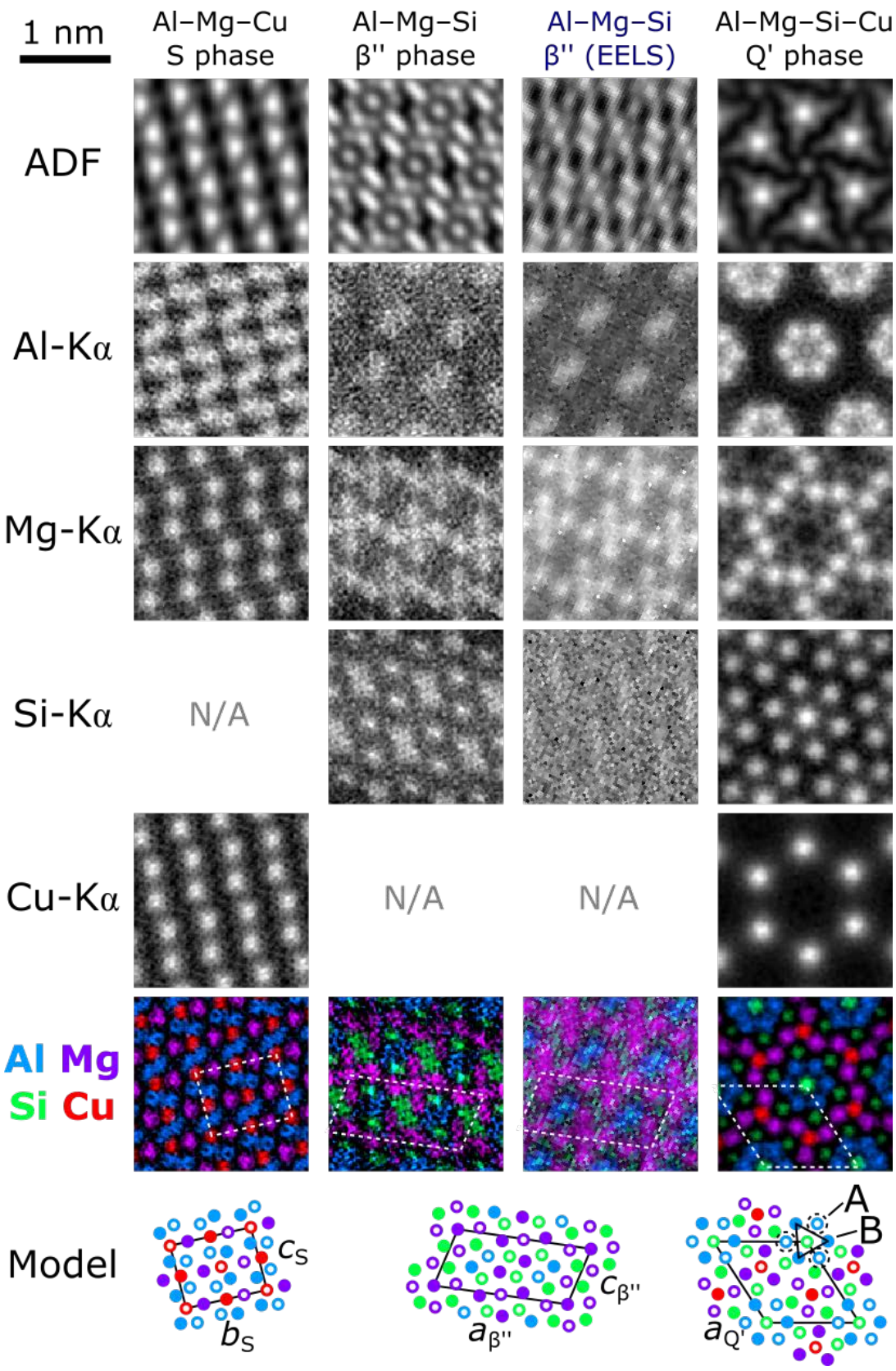

Figure 3: (Color online) Symmetry-averaged ADF and EDS images for three precipitates (S, β'' and Q' phases) in Al-Mg-(Si)-(Cu) alloys. EELS images from β'' are shown for comparison. All images are spatially averaged, and S/β'' are 2-fold rotation averaged, while Q' is 6-fold averaged. A common scale bar is given in the upper left corner. Color codes in the two last rows; blue = Al, purple = Mg,

green = Si, red = Cu. In the atomic models, filled (z=0) and empty circles (z=1/2) are separated by $a_{Al}/2$ = 202 pm in the paper normal direction.

While periodic averaging certainly is a useful technique, it can miss some important aperiodic features. As illustrated in Figure 4, the Q' dataset is indeed of sufficient quality for us to examine single atomic columns across the scanned area (e.g. the Cu-Kα map has SBR = 3.0, SNR = 2.9). Figure 4 shows the summed EDS maps of the Q' phase with no averaging over symmetries. The particle is uniform throughout the image, except for a few unit cells to the left, where a compositional change was observed. In the Q' model in Figure 3, the two sites labelled A and B are occupied by Al. In the marked areas in the Al map in Figure 4(b), only three out of these six sites are bright. In this part of the precipitate Al occupies either site A or B within one "ring" of Al/Mg columns, and transitions between A↔B occupation are evident in neighboring "rings". The remaining three columns are not present in the very clear Si and Cu maps, and should therefore be occupied by Mg. This is consistent with the change to a less bright atomic number contrast in the ADF images, and can be observed as a dark line marked in the overview image, Figure 4(j).

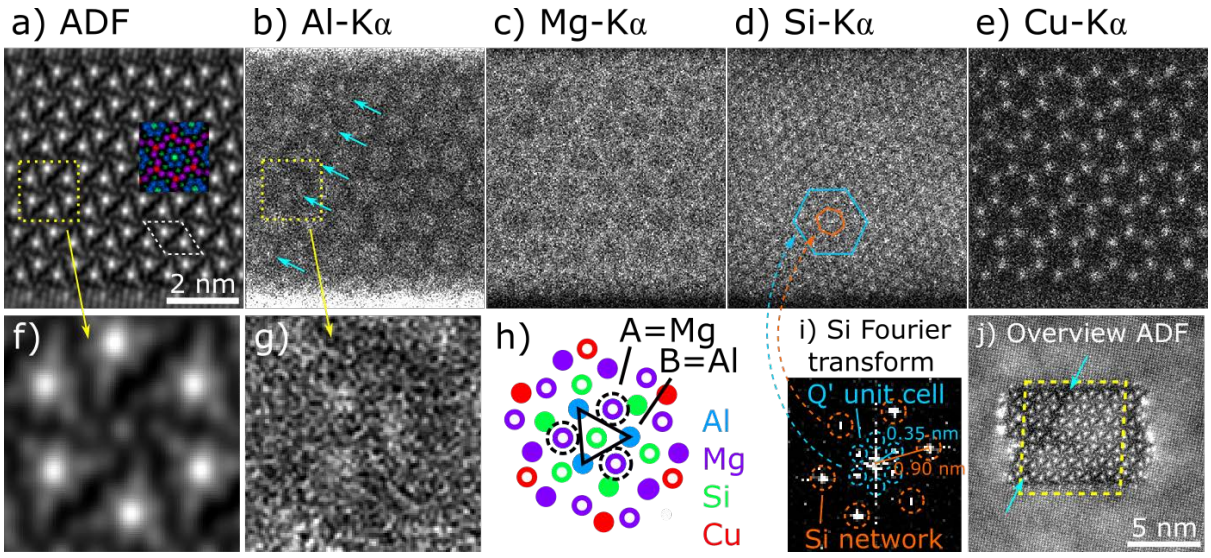

Figure 4: (Color online) (a–e) The full aligned and summed ADF and EDS images of the Q' phase in the Al–Mg–Si–Cu alloy. (f-h) Close-ups and model of an example area where the "Al ring" has composition Al_3Mg_3 instead of Al_6. (i) Fourier transform of the Si image. The inner spots arise from the intense Si columns at the corners of the Q' unit cell discussed in 4.2. (j) Overview image taken before the scan, showing a dark line where the structure is Mg-rich. The scan area is indicated with a yellow dashed square.

Figure 4(i) shows the Fourier transform of the Si image in (d). In addition to the clear hexagonal structure, a weaker, longer-range periodicity can be discerned. The spots correspond to the lattice parameter of the Q' phase, and are present because the Si atomic columns at the corners of the unit cells have a stronger signal than other Si columns, as seen in Figure 3. Cu is left as the only element which has a uniform intensity across all its designated columns.

4. Discussion

4.1. Resolution, signal and acquisition strategies

EDS maps such as those acquired in this study provides a good source of information about atomic structure. As in all EDS maps of thicker specimens, beam broadening, de-channeling and X-ray reabsorption add a lot of non-local information to the elemental maps (Spurgeon et al.). For these reasons, atomic column-wise quantitative composition measurements are difficult, although such feats have been achieved with careful modeling of the electron probe and its interaction with the specimen (Lu et al., 2013; Kothleitner et al., 2014).

When performing Gaussian fitting to the atomic columns in the summed ADF image of the S phase (Figure 1(d)), using the relative intensities of the three elemental species as fitting parameters, we measure a full width at half maximum of 205 pm. This corresponds to a Fourier spot resolution below 170 pm (ADF image Fourier transform included in the supplementary material). The resolution is slightly reduced from the ADF to the EDS images, to a full width at half maximum of 229 pm for Cu and 226 pm for Mg. The intrinsic EDX map resolution depends on various conditions, the most important being electron acceleration voltage, lens aberrations, and specimen thickness (which also increases with growing carbon contamination layers). By correcting focus between frames, and by using post-acquisition drift and distortion correction through non-rigid image registration, we have strongly reduced the degradation of resolution due to non-linear environmental scanning distortions, and specimen drift parallel to the electron beam.

Given that the noise in an EDS map is Poisson distributed, the SNR value of a summed elemental map should scale as the square root of the number of included frames. Figure 2(c) shows a good correspondence during the first half of the frames, before the sample experiences significant degradation. This finding is important, because it shows that if carbon contamination and sample damage can be controlled, our data processing methodology is capable of reaching the fundamental Poisson noise limited performance expected.

The final SNR of 1.18 is well below the atomic column visibility criterion value of 3 used by Lu et al., 2014b, and the noise would certainly prevent us from identifying each atomic column in Figure 1(e) if we did not know the structure to be periodic. In Figure 3, the Cu signal from the S phase is averaged over 126 atomic columns. Extrapolating the square root behavior, this averaging increases the SNR value to 13.2, which is well above the visibility criterion. The Cu map in Figure 4(e), which is not spatially averaged, has a SNR of 2.9, which barely reaches the requirement.

There are countless definitions of resolution and atomic column visibility, since the criteria for whether an atomic column is resolved or not are ultimately subjective and depends on what information one wishes to extract from an image. We will not attempt to create a new definition, but show the result of a Poisson noise simulation in Figure 5. The image quality of an example lattice is shown as a function of the column–column spacing and the number of X-ray counts per nm^2. The Gaussian full width at half maximum for each column is set to 240 pm, which is typical for our set-up. No X-ray background is assumed, and the contrast is adjusted to compensate for varying intensity modulation, counts and noise strength, to optimize the column visibility across the image. The figure shows the reason behind the apparent quality difference between the chemical maps in Figure 4: With slightly shorter column separations, the intensity difference between maxima and minima in the image is reduced, and a much higher dose is required to keep the SNR at the same level. This is crucial to consider when designing a new experiment, so that the required resolution is obtained through an adequate probe current, dwell time, number of frames and averaging scheme. Although increasing the total electron dose is the simplest way of increasing the X-ray signal, improving the EDS setup by

increasing the sensitivity or coverage area of the detector is preferable. For example, using dual Centurio detectors would double the number of X-ray counts (at 0° sample tilt) and improve atomically resolved EDS maps greatly (Kumamoto et al., 2016) without increasing the electron dose.

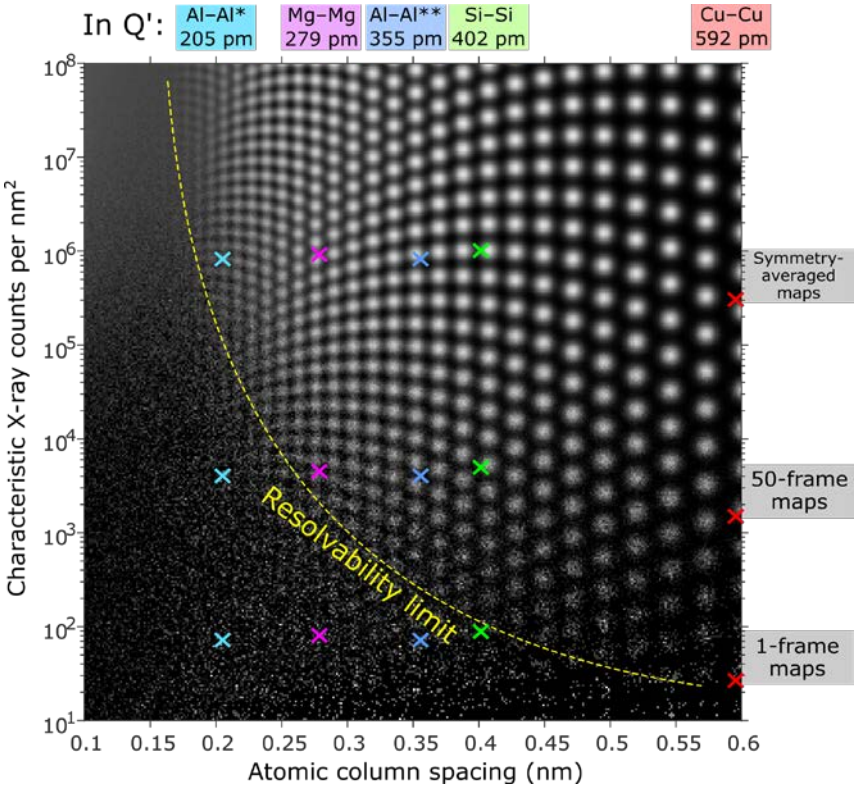

Figure 5: (Color online) Simulated Gaussian atomic columns in a lattice, with varying column spacing and applied Poisson noise. The probe size is 240 pm and the pixel size is 30 pm. The contrast is scaled to show the intensity variations optimally in all parts of the image. Column spacings in the Q' phase are displayed, with Al–Al spacings for the site occupations *A,B=Al, and **A=Al,B=Mg (see Figure 3). The crosses show the average counts measured inside the precipitate from our EDS maps of the Q' phase, e.g. from the 50-frame accumulated map in Figure 4.

Figure 2(a) displays a characteristic evolution of the carbon signal. The sudden onset after 10 minutes of beam exposure is consistent with a nucleation event, indicating that carbon atoms or hydrocarbons need time to diffuse toward the scanned area and establish a nucleus before amorphous carbon layer growth is energetically favorable. The saturation after a long time can arise either from re-sputtering of the deposited carbon, or simply depletion of the available carbon in the vicinity.

The degradation of the data-quality, as a result of carbon contamination and beam damage, slowly diminishes the intensities of the elemental peaks of interest in the X-ray spectrum. Although this inevitably causes the single-frame SNR to decrease, the SBR, which measures the contrast between atomic columns and the spaces in-between them, decreases little throughout one hour of scanning. This means that for the Al–Mg–Cu dataset, and certainly the others presented in this paper, no good is done by removing the "late" poorer-quality frames from the analysis. Indeed, we could have continued scanning for even longer times with incremental improvements to the summed EDS image, as long as the lattice is visible in the ADF frames for use in the Smart Align algorithm for alignment of the image series. A hard limit to the scanning time (and electron dose) at which no more information is obtained, is the point at which structural changes such as amorphization or solid dissolution

happens. Beyond this one would no longer be scanning the same atomic structure. Judging by the ADF images acquired after the EDS mapping (found in the Supplementary material), we are safely below this limit.

The ratio between the elemental peaks in Figure 2(a) does not remain constant throughout the acquisition, which is why we have not attempted any sort of quantification of the summed EDS volumes. The explanation for this is not completely clear: If the precipitate is sputtered, the signals from Al, Mg and Cu should decrease at similar rates. A small area of Al matrix (which is less beam sensitive) outside the precipitate is included in the scan, and limits the decrease of the Al signal somewhat. It is also possible that the Al is not sputtered away, but instead remains as part of an ever-growing aluminium oxide surface layer above and below the precipitate.

In cases where the material is very beam-sensitive, one strategy to minimize sample damage and maximize the amount of high-quality signal, would be to scan many identical particles and accumulate signal across them. The operator should assure that the geometry and scan direction are matched, though for the precipitate types studied here, the intrinsic orientation relationship with Al is of great help. For larger particles/crystal grains where a large continuous area can be scanned, the accumulation of adequate EDS counts becomes an easier task.

The inability to unambiguously determine the site which solute Zn atoms occupy in the S phase, even with symmetry-averaging, highlights an important limitation to EDS mapping performed at reasonable dose levels: we cannot detect whether elements mix into other columns in small amounts, but only conclude on which elemental species is the dominant one for a given column.

In summary, the approach for atomic-resolution EDS mapping must be tailored to the specimen and the information to be obtained. We have used a specimen area with a thickness of 30–40 nm, which is thicker than is obtainable near the specimen edge, in order to increase the signal without much degradation of resolution. An acceleration voltage of 80 kV was selected as 200 kV would quickly damage the studied precipitates. The 34 mrad convergence angle was selected to maximize the signal and obtain a high resolution, though a lower angle could increase the SBR of the maps (Dycus et al., 2016; Chen et al., 2016). Similarly, a probe current producing the highest possible signal and still giving the required resolution was chosen. The pixel size is $1/8^{th}$ of the probe FWHM, which is appropriate for separating the noise from the resolved features. With these parameters and the procedure of post-acquisition non-rigid alignment of multi-frame EDS maps, high-quality elemental maps can be created, with Figure 5 serving as a guide to the expected resolution estimated from the accumulated number of characteristic X-ray counts.

4.2. Chemistry in the mapped precipitates

The three precipitate phases investigated in this study are fully coherent along their main growth directions, which is also the electron beam direction. Atomic columns therefore generally have a repeat distance of a_{Al} = 405 pm. With all columns having the same repeat distance, the compositions can be inferred directly by counting atoms in the projected unit cell models in Figure 3. The model of the S phase is consistent with the Perlitz–Westgren model with composition Al_2MgCu and space group $Cmcm$ (Perlitz and Westgren, 1943). The β'' phase matches well with the model of Hasting et al., having composition $Al_2Mg_5Si_4$ and space group $C2/m$ (Hasting et al., 2009). The results were consistent between EELS and EDS, although atomic columns were not visible in the Si-K EELS map. Mørtsell et al., 2016, have successfully mapped Si columns with separation 0.4 nm using the same EELS setup, but at a higher voltage of 200 kV.

The Al–Mg–Si–Cu dataset will be discussed in further detail as some interesting details are discernable. The Q' phase, which is isostructural to the equilibrium Q phase, seems from our symmetry-averaged images to have a composition $Al_6Mg_6Si_7Cu_2$. This fits with the compositional framework found for the Q phase by X-ray diffraction, $Al_xMg_{12-x}Si_7Cu_2$ (Arnberg and Aurivillius, 1980), with $x = 6$. Density functional theory calculations have given a different composition of minimized enthalpy for both Q and Q', $Al_3Mg_9Si_7Cu_2$ ($x = 3$) (Wolverton, 2001; Ravi and Wolverton, 2004). More precisely, the discrepancy is located at the Q' sites labelled A and B in Figure 3. The two sites are equivalent, and our symmetry-averaged map indicates that they are both occupied by Al, except for certain areas, where A=Al and B=Mg (or vice versa), in agreement with Wolverton's calculations. In the quantitative nano-beam diffraction (NBD) studies of Torsæter et al., 2008, the sites A and B were estimated to both contain 50% Al and Mg. It must be noted that NBD gives an average over many unit cells, while atomic-resolution microscopy is able to pick up subtle variations locally. The composition of the A and B sites are probably controlled by the amount of available Mg in solid solution during precipitation. Irrespective of the occupation of the A and B sites, the space group of Q' is $P\bar{6}$.

The symmetry-averaged Si image in Figure 3 also provides some interesting information. The Si column at the projected 3/6-fold rotation center in the Q' phase has a particularly intense Si-Kα signal. Gaussian fitting to atomic columns (after subtraction of the constant background) gives a 31% stronger integrated signal for these columns than for the other Si columns. This leads to a periodicity with the Q' lattice parameters, measurable on a Fourier transform of the full Si image (see Figure 4(i)). One could think that the columns with weaker intensity contain vacancies or other elemental species. However, Si columns in other precipitate phases such as β' and B' have been found to have a shorter repeat distance than a_{Al}, in the form $n/(n+1) \times a_{Al}$ for some whole number n (n = 3 for β' (Vissers et al., 2007) and n = 5 for B' (Vissers et al., 2008). This generates a superstructure in the main growth direction (normal to the imaged planes in this work), with a lattice parameter of $n \times a_{Al}$. The phenomenon has been noticed both through a difference in Si column intensity in ADF-STEM images, and through the presence of super-reflections in NBD patterns (Vissers et al., 2008). A superstructure is therefore most probable explanation.

A tighter spacing of one of the 7 Si columns changes the composition to $Al_xMg_{12-x}Si_{7+1/n}Cu_2$. Since Q' is otherwise isostructural to the B' phase (Marioara et al., 2007), n should assume the value 5 (Vissers et al., 2008), which yields $Si_{7.2}$. Interestingly, if the Si column was doubly occupied (n = 1) and A,B=Al, the structure would have a complete 6-fold screw axis, giving it the space group $P6_3$.

5. Conclusion

Precipitate particles in aluminium alloys are some of the more challenging objects that have been studied using high-resolution STEM-EDS thus far, due to their small size, instability under the electron beam and frequent carbon build-up during scanning. EDS imaging has been demonstrated with atomic resolution despite these difficulties, and typically produces better results than EELS for specimens that are thick and/or susceptible to carbon contamination. Our chosen method of rigorous post-realignment of each acquired image frame, rather than simple drift correction during scanning, also better mitigates many probe-related problems including scanning distortions and focus/stigmatism drift.

Lattice averaging, exploiting periodic and rotational symmetries, is very useful for finding the compositions of each atomic site in the unit cell of a multi-element phase. In this manner the compositions of the S and β'' phases were determined to Al_2MgCu and $Al_2Mg_5Si_4$, respectively. In a variety of cases, we also have enough signal in an EDS image to identify the element of single atomic columns in the image. In particular, we observed a transition in the Q' phase between unit cells of

compositions $Al_xMg_{12-x}Si_7Cu_2$ with $x = 6$ and $x = 3$, with $x = 6$ being most common configuration. Differences between Si column intensities in the same phase reveal a fractional occupancy which signifies a superstructure in the main growth direction of the particle, and a composition with a slightly increased amount of Si, $Al_6Mg_6Si_{7.2}Cu_2$.

The exact compositions of precipitates are important to know as a part of the design of alloy compositions and heat treatments that optimize the size, distribution and type of strengthening precipitates. The phases investigated in this paper are ordered and stoichiometric; further work includes mapping disordered precipitates with no projected symmetries (but still having well-defined atomic columns). Absolute composition quantification will also be developed to investigate precipitates which may have several elements present in any given column.

Acknowledgments

The authors would like to thank the Research Council of Norway (RCN) for funding of the FRINATEK project “Fundamental investigations of precipitation in the solid state with focus on Al-based alloys”. The TEM work was carried out on the NORTEM instrument JEOL ARM-200F, TEM Gemini Centre, Norwegian University of Science and Technology (NTNU), Norway. The research leading to these results has received funding from the European Union Seventh Framework Programme under Grant Agreement 312483 - ESTEEM2 (Integrated Infrastructure Initiative–I3).

References

Allen, L.J., Findlay, S.D., Oxley, M.P., Rossouw, C.J., 2003. Lattice-resolution contrast from a focused coherent electron probe. Part I. Ultramicroscopy 96, 47–63.

Allen, L.J., D'Alfonso, A.J., Findlay, S.D., 2015. Modelling the inelastic scattering of fast electrons. Ultramicroscopy 151, 11–22.

Arnberg, L., Aurivillius, B., 1980. The crystal structure of $Al_xCu_2Mg_{12-x}Si_7$, (h-AlCuMgSi). Acta Chem. Scand. 34A, 1–5.

Bjørge, R., Andersen, S.J., Marioara, C.D., Etheridge, J., Holmestad, R., 2012. Scanning transmission electron microscopy investigation of an Al–Mg–Si–Ge–Cu alloy. Phil. Mag. 92, 3983–3993.

Chen, J.H., Costan, E., van Huis, M.A., Xu, Q., Zandbergen, H.W., 2006. Atomic Pillar-Based Nanoprecipitates Strengthen AlMgSi Alloys. Science 312, 416–419.

Chen, Z., Weyland, M., Sang, X., Xud, W., Dycus, J.H., LeBeau, J.M., D'Alfonso, A.J., Allen, L.J., Findlay, S.D., 2016. Quantitative atomic resolution elemental mapping via absolute-scale energy dispersive X-ray spectroscopy. Ultramicroscopy 168, 7–16.

Chu, M.-W., Liou, S.C., Chang, C.-P., Choa, F.-S., Chen, C.H., 2010. Emergent Chemical Mapping at Atomic-Column Resolution by Energy-Dispersive X-Ray Spectroscopy in an Aberration-Corrected Electron Microscope. Phys. Rev. Lett. 104, 196101.

D'Alfonso, A.J., Freitag, B., Klenov, D., Allen, L.J., 2010. Atomic-resolution chemical mapping using energy-dispersive x-ray spectroscopy. Phys. Rev. B 81, 100101.

Dycus, J.H., Xu, W., Sang, X., D'Alfonso, A.J., Chen, Z., Weyland, M., Allen, L.J., 2016. Influence of experimental conditions on atom column visibility in energy dispersive X-ray spectroscopy. Ultramicroscopy 171, 1–7.

Ehlers, F.J.H., Wenner, S., Andersen, S.J., Marioara, C.D., Lefebvre, W., Boothroyd, C.B., Holmestad, R., 2014. Phase stabilization principle and precipitate-host lattice influences for Al–Mg–Si–Cu alloy precipitates. J. Mater. Sci. 49, 6413–6426.

Feng B., Yokoi, T., Kumamoto, A., Yoshiya, M., Ikuhara, Y., Shibata, N., 2016. Atomically ordered solute segregation behaviour in an oxide grain boundary. Nature Comms. 7, 11079.

Hasting, H.S., Frøseth, A.G., Andersen, S.J., Vissers, R., Walmsley, J.C., Marioara, C.D., Danoix, F., Lefebvre, W., Holmestad, R., 2009. Composition of β'' precipitates in Al–Mg–Si alloys by atom probe tomography and first principles calculations. J. Appl. Phys. 106, 123527.

Jeong, J.S., Mkhoyan, K.A., 2016. Correlation Averaging of Single-Atomic-Column STEM-EDX Images for Sub-Atomic Information. Microsc. Microanal. 22, 882–883.

Jones, L., Yang, H., Pennycook, T.J., Marshall, M.S.J., van Aert, S., Browning, N.D., Castell, M.R., Nellist, P.D., 2015. Smart Align—a new tool for robust non-rigid registration of scanning microscope data. Adv. Struct. Chem. Imaging 1, 8.

Kilaas, R., Radmilovic, V., 2001. Structure determination and structure refinement of Al_2CuMg precipitates by quantitative high-resolution electron microscopy. Ultramicroscopy 88, 63-72.

Klenov, D.O., Zide, J.M.O, 2011. Structure of the InAlAs/InP interface by atomically resolved energy dispersive spectroscopy. Appl. Phys. Lett. 99, 141904.

Kothleitner, G., Neish, M.J., Lugg, N.R., Findlay, S.D., Grogger, W., Hofer, F., Allen, L.J., 2014. Quantitative Elemental Mapping at Atomic Resolution Using X-Ray Spectroscopy. Phys. Rev. Lett. 112, 085501.

Kumamoto, A., Shibata, N., Nayuki, K., Tohei, T., Terasaki, N., Nagatomo, Y., Nagase, T., Akiyama, K., Kuromitsu, Y., Ikuhara, Y., 2016. Atomic structures of a liquid-phase bonded metal/nitride heterointerface. Sci. Rep. 6, 22936.

Li, K., Béché, A., Song, M., Sha, G., Lu, X., Zhang, K., Du, Y., Ringer, S.P., Schryvers, D., 2014. Atomistic structure of Cu-containing β'' precipitates in an Al–Mg–Si–Cu alloy. Scripta Mater. 75, 86–89.

Liu, Z.R., Chen, J.H., Wang, S.B., Yuan, D.W., Yin, M.J., Wu, C.L., 2011. The structure and the properties of S-phase in AlCuMg alloys. Acta Mater. 59, 7396–7405.

Lu, P., Xiong, J., van Benthem, M., Jia, 2013. Atomic-scale chemical quantification of oxide interfaces using energy-dispersive X-ray spectroscopy. Q., Appl. Phys. Lett. 102, 173111.

Lu, P., Zhou, L., Kramer, M.J., Smith, D.J., 2014a. Atomic-scale Chemical Imaging and Quantification of Metallic Alloy Structures by Energy-Dispersive X-ray Spectroscopy. Sci. Rep. 4, 3945.

Lu, P., Romero, E., Lee, S., MacManus-Driscoll, J.L., Jia, Q., 2014b. Chemical Quantification of Atomic-Scale EDS Maps under Thin Specimen Conditions. Microsc. Microanal. 20, 1782–1790.

Lu, P., Yuan, R.L., Ihlefeld, J.F., Spoerke, E.D., Pan, W., Zuo, J.M., 2016. Fast Atomic-Scale Chemical Imaging of Crystalline Materials and Dynamic Phase Transformation. Nano Lett. 16, 2728–2733.

Marioara, C.D., Andersen, S.J., Stene, T.N., Hasting, H., Walmsley, J., van Helvoort, A.T.J., Holmestad, R., 2007. The effect of Cu on precipitation in Al–Mg–Si alloys. Phil. Mag. 87, 3385–3413.

Marioara, C.D., Lefebvre, W., Andersen, S.J., Friis, J., 2013. Atomic structure of hardening precipitates in an Al–Mg–Zn–Cu alloy determined by HAADF-STEM and first-principles calculations: relation to η-$MgZn_2$. J. Mater. Sci. 48, 3638–3651.

Marlaud, T., Deschamps, A., Bley, F., Lefebvre, W., Baroux, B., 2010. Influence of alloy composition and heat treatment on precipitate composition in Al–Zn–Mg–Cu alloys. Acta Mater. 58, 248–260.

Mondolfo, L.F., 1976. Aluminum alloys: structure and properties, Butterworths, London.

Mørtsell, E.A., Wenner, S., Longo, P., Andersen, S.J., Marioara, C.D., Røyset, J., Holmestad, R., 2016. Elemental electron energy loss mapping of a precipitate in a multi-component aluminium alloy. Micron 86, 22–29.

Ninive, P.H., Strandlie, A., Gulbrandsen-Dahl, S., Lefebvre, W., Marioara, C.D., Andersen, S.J., Friis, J., Holmestad, R., Løvvik, O.M., 2014. Detailed atomistic insight into the β'' phase in Al–Mg–Si alloys. Acta Mater. 69, 126–134.

Pennycook, S.J., 2012. Seeing the atoms more clearly: STEM imaging from the Crewe era to today. Ultramicroscopy 123, 28–37.

Perlitz, H., Westgren, A., 1943. The crystal structure of Al_2CuMg. Ark. kemi Mineral Geol. 16B, 1–5.

Ravi, C., Wolverton, C., 2004. First-principles study of crystal structure and stability of Al–Mg–Si–(Cu) precipitates. Acta Mater. 52, 4213–4227.

Spurgeon, S.R., Du, Y., Chambers, S.A., Measurement Error in Atomic-Scale STEM-EDS Mapping of a Model Oxide Interface, arXiv preprint arXiv:1610.03432 (submitted to Microsc. Microanal).

Torsæter, M., Vissers, R., Marioara, C.D., Andersen, S.J., Holmestad, R., 2008. Crystal Structure Determination of the Q' and C-type Plate Precipitates in Al-Mg-Si-Cu (6xxx) Alloys, in Aluminium alloys: Their Physical and Mechanical Properties, vol. 2, edited by Jürgen Hirsch, Birgit Skrotzki and Günter Gottstein.

Vissers, R., van Huis, M.A., Jansen, J., Zandbergen, H.W., Marioara, C.D., Andersen, S.J., 2007. The crystal structure of the β'' phase in Al–Mg–Si alloys. Acta Mater. 55, 3815–3823.

Vissers, R., Marioara, C.D., Andersen, S.J., Holmestad, R., 2008. Crystal Structure determination of the B' phase in Al-Mg-Si Alloys by combining Quantitative Electron diffraction and ab initio Calculations, in Aluminium alloys: Their Physical and Mechanical Properties, vol. 2, edited by Jürgen Hirsch, Birgit Skrotzki and Günter Gottstein.

Williams, D.B., Carter, C.B., 2009. Transmission Electron Microscopy: A Textbook for Materials Science, 2nd edition, Springer.

Wenner, S., Friis, J., Marioara, C.D., Holmestad, R., 2016. Precipitation in a mixed Al–Cu–Mg/Al–Zn–Mg alloy system. J. Alloy. Compd. 684, 195–200.

Wolverton, C., 2001. Crystal structure and stability of complex precipitate phases in Al–Cu–Mg–(Si) and Al–Zn–Mg alloys. Acta Mater. 49, 3129–3142.

Yankovich, A.B., Zhang, C., Oh, A., Slater, T.J.A., Azough, F., Freer, R., Haigh, S.J., Willet,t R., Voyles, P.M., 2016. Non-rigid registration and non-local principle component analysis to improve electron microscopy spectrum images. Nanotechnology 27, 364001.

Zandbergen, H.W., Andersen, S.J., Jansen, J., 1997. Structure Determination of Mg_5Si_6 Particles in Al by Dynamic Electron Diffraction Studies. Science 277, 1221–1225.

Atomic-resolution chemical mapping of ordered precipitates in Al alloys using energy-dispersive X-ray spectroscopy (Supplementary material)

Alloy preparation

All alloys were cast to billets, homogenized and extruded to cylindrical bars with 20 mm diameter. Various heat treatments were applied to obtain the desired phases at suitable sizes and distributions:

- The Al–Mg–Cu alloy was given a solution heat treatment (SHT) at 440 °C for 1 hour, then water quenched (WQ) and aged at 150 °C for 8 days.
- The Al–Mg–Si alloy was given a SHT at 535 °C for 5 minutes, WQ, kept at room temperature (RT) for 4 hours, heated at an average rate of 26 °C per hour to 195 °C and kept at this temperature for 4 hours.
- The Al–Mg–Si–Cu alloy was given an SHT at 530 °C for 30 min, WQ, kept at RT for 4 hours, aged at 155 °C for 12 hours and over-aged at 200 °C for 21 days.

Foils with thickness of 50–100 µm were prepared from each alloy, with the surface normal in the extrusion direction, for easy location of $<001>_{Al}$ grains. Electropolishing was done with a Struers TenuPol-5 using a solution of 1/3 nitric acid and 2/3 methanol, kept at −25 °C. A voltage of 20 V was applied. All samples were plasma cleaned for 2 minutes before insertion into the microscope.

ADF images

Figures S1–S3 show the first and last ADF frame of each dataset, and overview ADF images taken after the EDS scans. In Figure S1 and S2, carbon contamination is the main mechanism for degradation of the sample. In Figure S3, some sputtering has occurred, and Cu seems to have segregated to the Al lattice outside the precipitate–matrix interface.

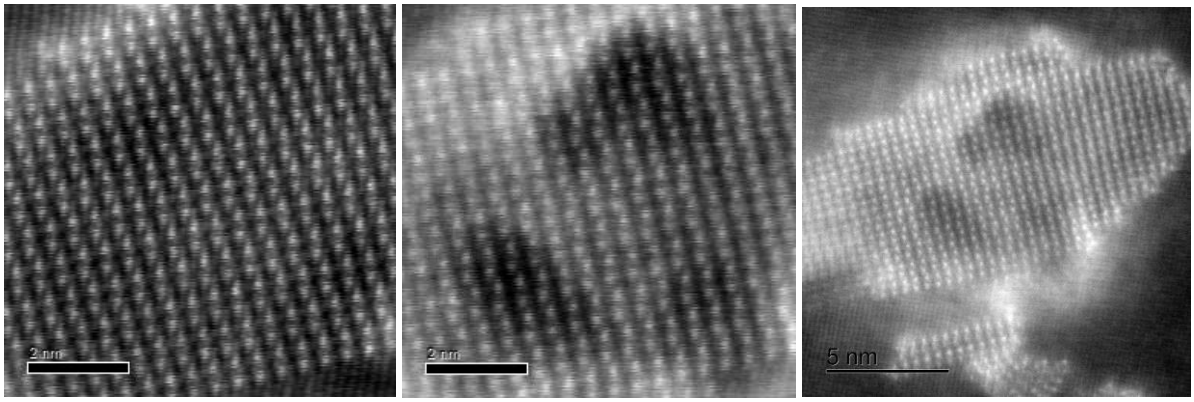

Figure S1: ADF images from the Al–Mg–Cu alloy. Frame 1, frame 50 and after-image.

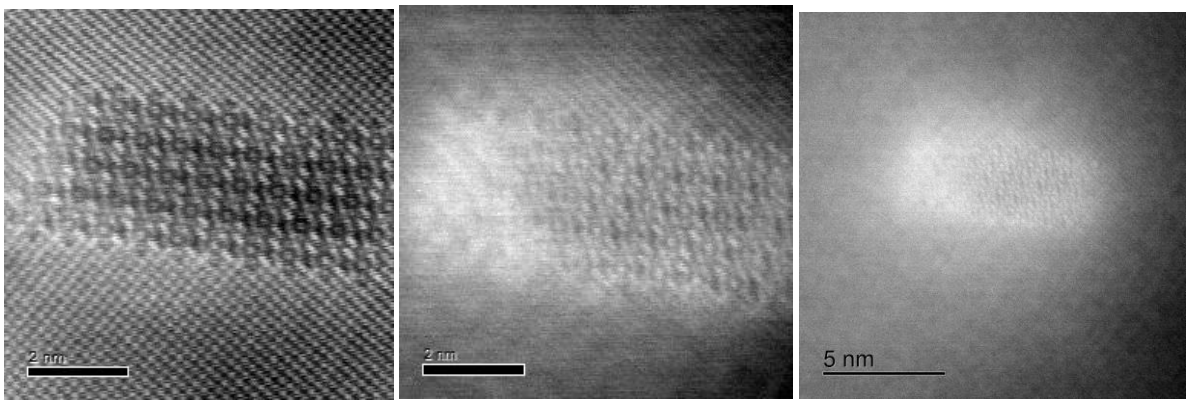

Figure S2: ADF images from the Al–Mg–Si alloy. Frame 1, frame 30 and after-image.

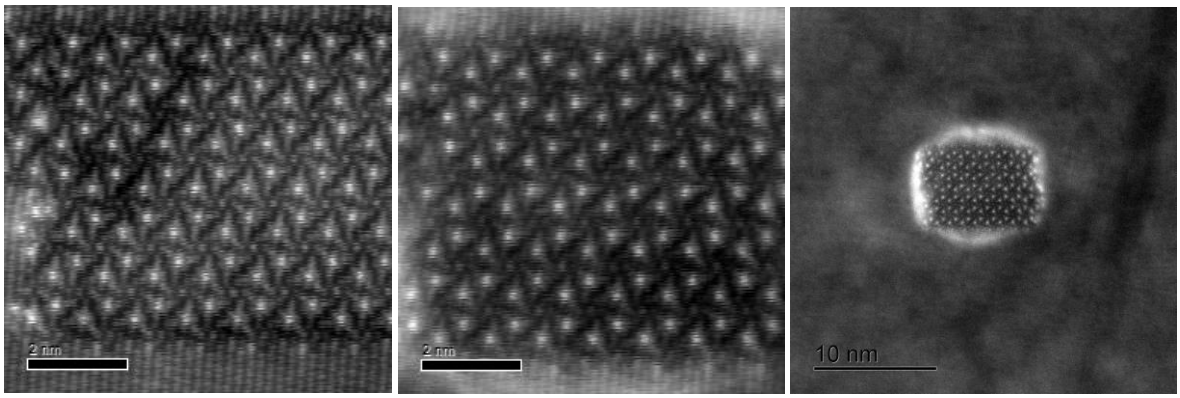

Figure S3: ADF images from the Al–Mg–Si–Cu alloy. Frame 1, frame 50 and after-image.

Full EDS maps

The two full EDS maps not shown in the main manuscript are displayed in Figures S4 and S5. All EDS images are constructed from Kα peaks integrated to full width at one-third maximum. The aligned and summed EDS volume was cropped to only contain areas that are present in all frames.

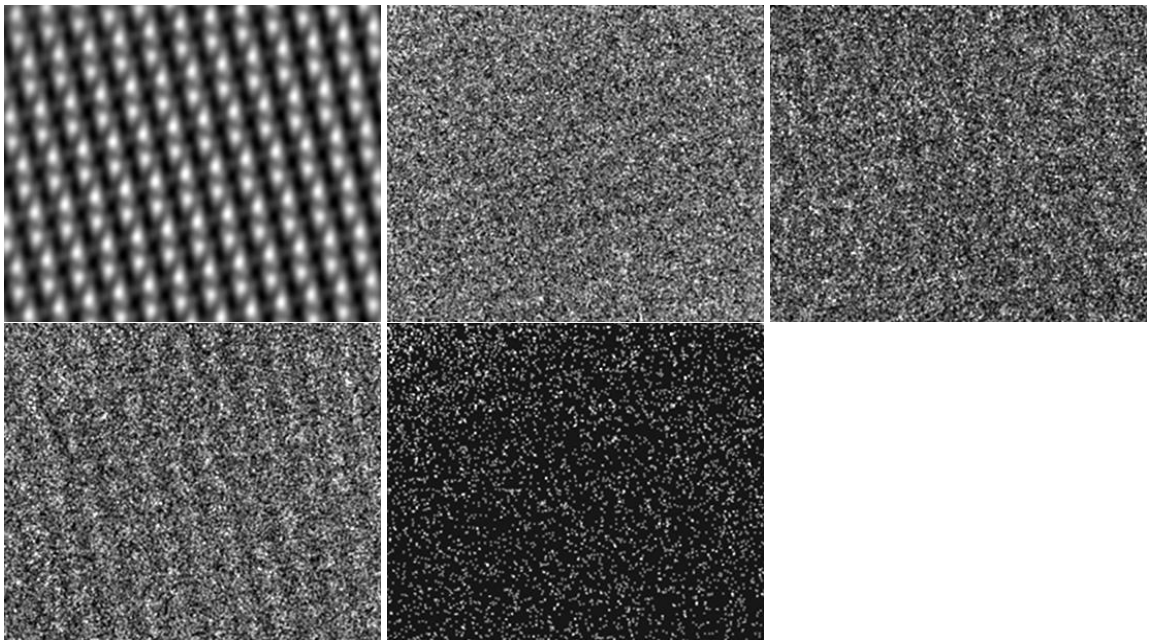

Figure S4: The summed maps of the Al–Mg–Cu sample. From the left: ADF, Al, Mg, Cu, Zn.

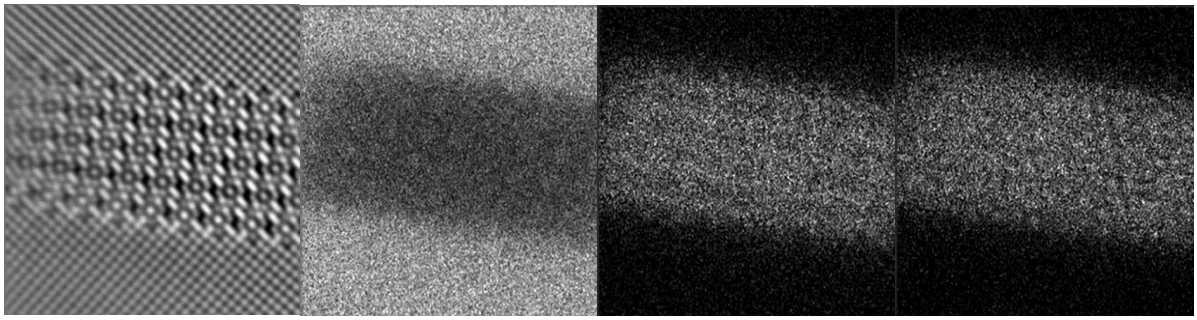

Figure S5: The summed maps of the Al–Mg–Si sample. From the left: ADF, Al, Mg, Si.

Full EDS spectra

Figure S6 shows the summed spectra from the three obtained datasets, within the areas shown in Figure 4, S4 and S5. The energy range was reduced in the Al–Mg–Si case as all the relevant elements have characteristic X-ray peaks at low energies. The characteristic peaks used for analysis have black labels while other identified peaks have grey labels. The Fe and Co signals stem from stray radiation from the microscope polepiece.

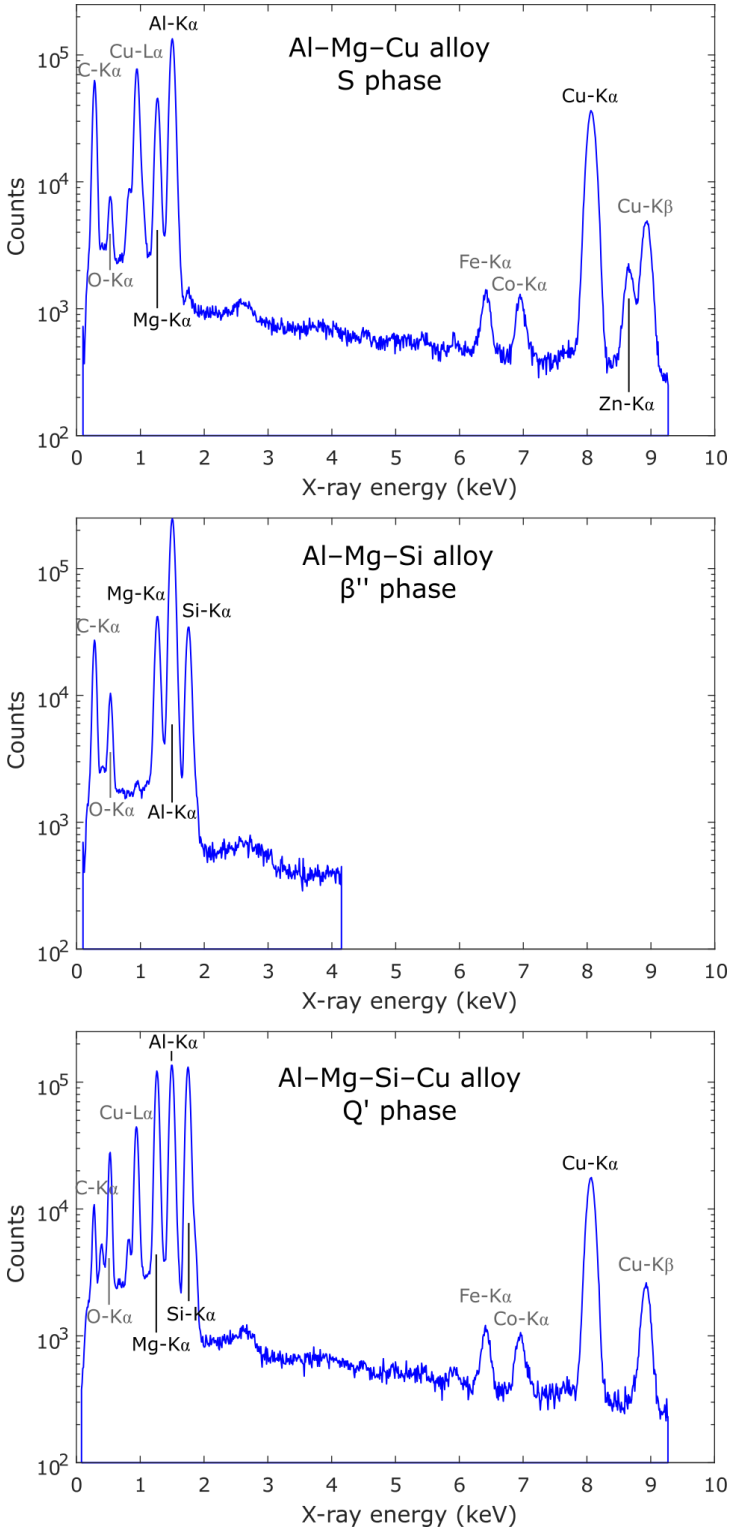

Figure S6: The summed EDS spectra from the three presented datasets.

EELS ADF images, maps and spectrum

Figure S7 shows the precipitate used for the EELS data acquisition. The right part of the particle is the β'' phase, while the left part is disordered and was not included in the symmetry-averaged maps.

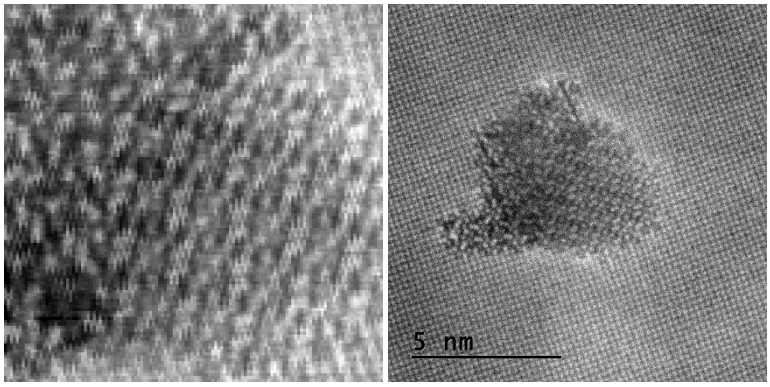

Figure S7: EELS acquisition of the Al–Mg–Si sample. (left) simultaneous ADF image, (right) after-image.

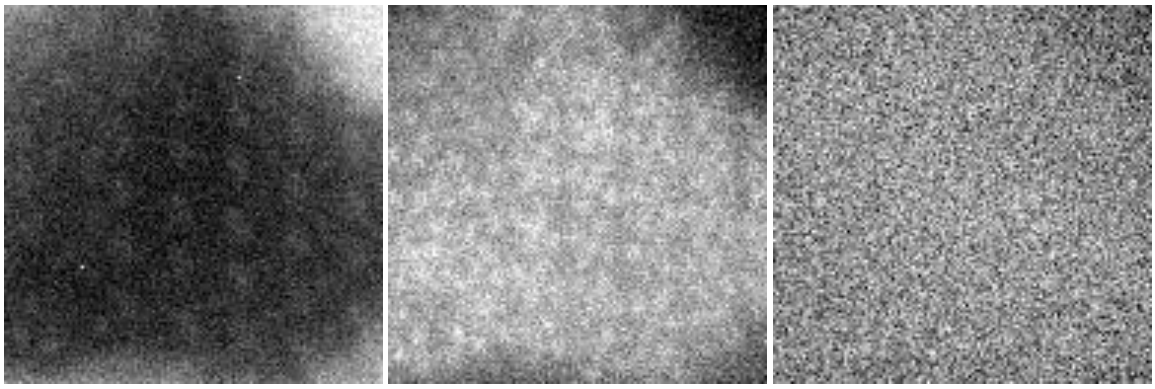

Figure S8: EELS elemental maps from the Al–Mg–Si sample. From the left: Al-K, Mg-K, Si-K.

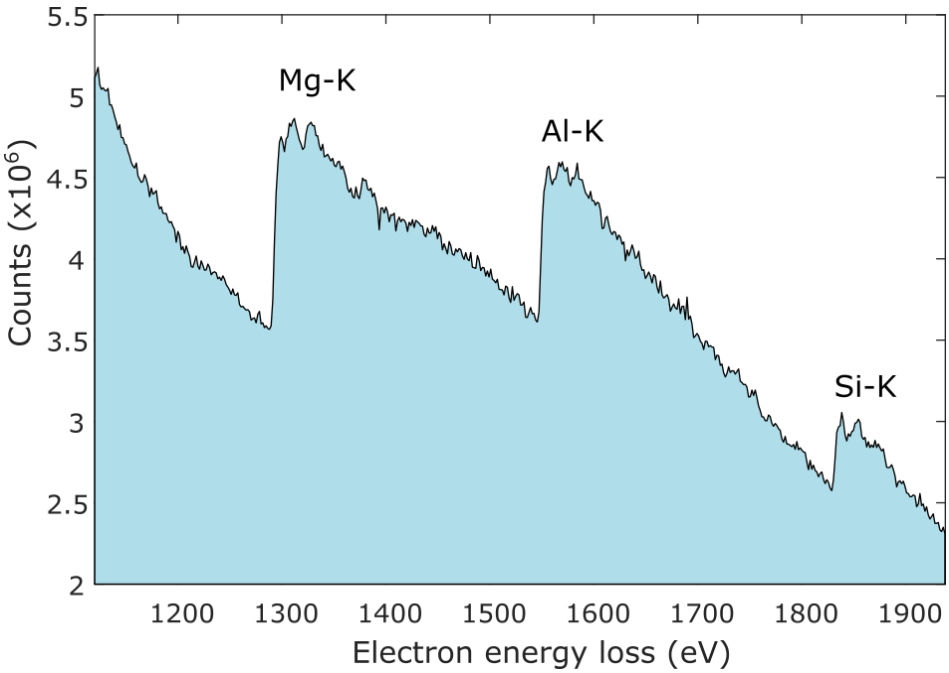

Figure S9: The summed high-loss EELS spectrum, showing the three edges of interest.

Resolution/signal/noise analysis

Figures S10–S12 shows the results from the signal/noise separation for the Al–Mg–Cu and Al–Mg–Si–Cu datasets. A sum of atomic column-centered Gaussians with full widths at half maximum of 229 pm and 242 pm (respectively) was the least squares fit to the summed Cu-Kα images. The residual after Gaussian subtraction still shows some lattice information, which can have two reasons: (i) A Gaussian distribution does not perfectly describe the X-ray intensity distribution around an atomic column. (ii) Uniform Gaussian heights were assumed, while the Cu signal at atomic positions in reality vary in intensity across the image. Some remaining signal is included in what we define as the noise component, which leads to a slight underestimation of the signal/noise ratio. For comparison with the Fourier spot visibility (a common method of estimating resolution), the Fourier transform of the Al–Mg–Cu ADF image is shown in Figure S13.

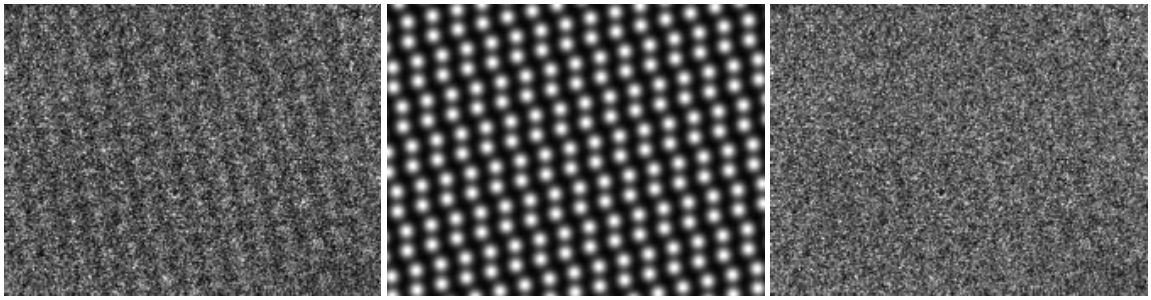

Figure S10: Gaussian fitting to the S phase structure in the Al–Mg–Cu alloy. (left) Summed Cu-Kα image. (middle) The best-fit Gaussian distributions. (right) The residual after subtracting (middle) from (left), defined as the noise.

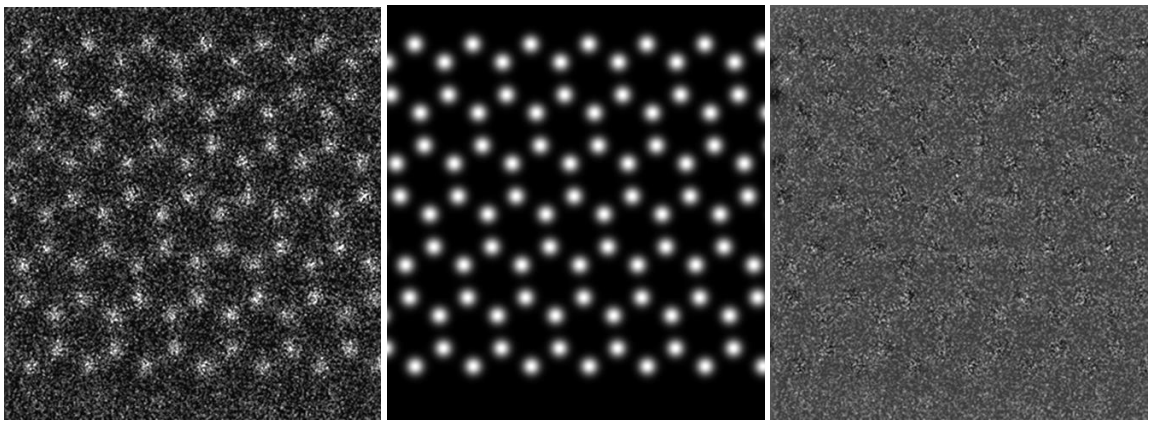

Figure S11: Gaussian fitting to the Q' phase structure in the Al–Mg–Si–Cu alloy. (left) Summed Cu-Kα image. (middle) The best-fit Gaussian distributions. (right) The residual after subtracting (middle) from (left), defined as the noise.

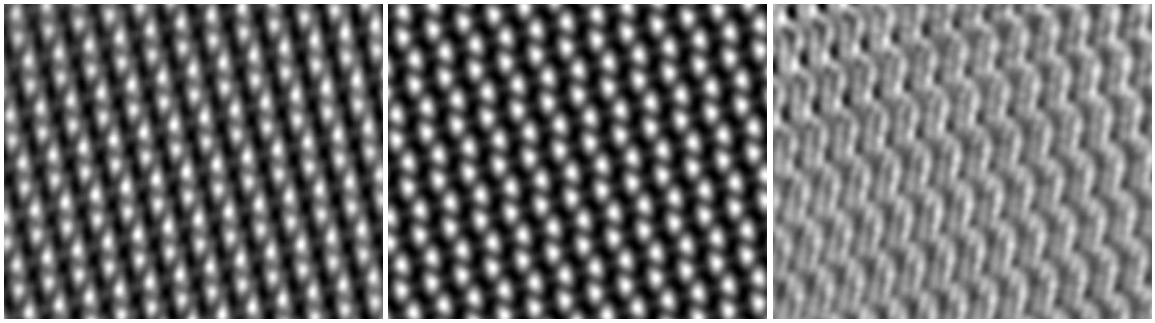

Figure S12: Gaussian fitting to the ADF image of the S phase structure. (left) Summed ADF image. (middle) The best-fit Gaussian distributions. (right) The residual after subtracting (middle) from (left), defined as the noise. The reason for the strong regularity in the noise could be probe astigmatism or a slight misorientation of the sample.

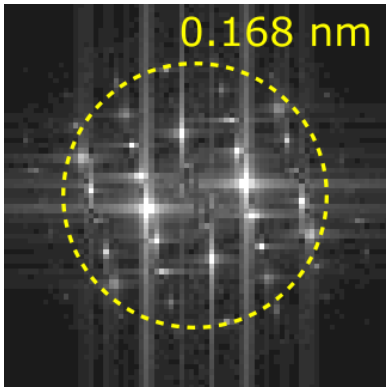

Figure S13: The Fourier transform of the ADF image of the S phase, for measurement of Fourier spot resolution. All clearly visible spots are included in the dashed circle.

Image simulation

Below is the Matlab code used to create Figure 5.

```
% Atomic column visibility and resolution test

% Adjustable parameters
Nx = 10; % Field of view in nm
Ny = 10;
pix = 0.03; % Pixel size in units of nm
probesize = 0.24; % Full width at half maximum
spacing_max = 0.6; % nm
spacing_min = 0.1; % nm
counts_exponent_max = 8; % The counts per nm^2 varies between 10^counts_exponent_min and 10^counts_exponent_max
counts_exponent_min = 1;

% Create pixel grid
[x,y] = meshgrid(0:pix:Nx,0:pix:Ny);
[points_y,points_x] = size(x);

% Position variation in properties
spacing = x/Nx*(spacing_max - spacing_min) + spacing_min; % x-variation in y-spacing
sigma = probesize/2.3548; % Formula from Wolfram Mathworld
sigma2 = sigma.^2;
cpnm = 10.^(y/Ny*(counts_exponent_max-counts_exponent_min)+counts_exponent_min); % Counts per nm
counts = cpnm * pix^2; % Counts per pixel

% Generate Gaussian positions
Ng = 0; % Number of Gaussians in image
g_x = zeros(1,10000);
g_y = zeros(1,10000);
ax = -1; % The first Gaussian is 1nm before the image border
while ax < Nx + 1
    ay = -1; % The first Gaussian is 1nm before the image border
    while ay < Ny + 1
```

```
        Ng = Ng + 1;
        g_x(Ng) = ax;
        g_y(Ng) = ay;
        ay = ay + ax/Nx*(spacing_max - spacing_min) + spacing_min; % Variable
y-spacing
    end
    ax = ax + ax/Nx*(spacing_max - spacing_min) + spacing_min;
end

% Add up Gaussian signals (with 2D normal distribution normalization)
signal = zeros(points_y,points_x);
for gi = 1:Ng
    signal = signal + exp(-0.5*((x-g_x(gi)).^2 + (y-g_y(gi)).^2)./sigma2) ./
(2*pi*sigma2);
end
signal = signal .* counts;

% Noise addition (requires the Image processing toolbox)
image = 1.0e+12*imnoise(signal*1.0e-12,'poisson');

% Contrast correction, compensating for intensity of added-up Gaussians and
Poisson noise
c_min = zeros(points_y,points_x);
c_max = zeros(points_y,points_x);
num_contrast_gaussians = 20; % Must be even, and large enough for extreme
precision with short column separations
for ax = 1:num_contrast_gaussians
    for ay = 1:num_contrast_gaussians
        % Intensity between Gaussians
        c_min = c_min + exp(-0.5*((num_contrast_gaussians/2+0.5-ax).^2 +
(num_contrast_gaussians/2+0.5-ay).^2).*spacing.^2./sigma2)               ./
(2*pi*sigma2);
        % Intensity on top of a Gaussian
        c_max = c_max + exp(-0.5*((num_contrast_gaussians/2-ax).^2 +
(num_contrast_gaussians/2-ay).^2).*spacing.^2./sigma2) ./ (2*pi*sigma2);
    end
end
c_max = 1.1*c_max .* (counts+sqrt(counts));
c_min = c_min .* (counts); % Optimized for short spacing resolvability
%c_min = 0; % Optimized for similar-looking atomic columns
image_n = (image - c_min) ./ (c_max - c_min);

% Display the figure and write to an image file
figure
imshow(image_n)
imwrite(image_n,'acv.bmp','bmp')
figure
surf(spacing,cpnm,image_n)
%daspect([spacing_max-spacing_min,cpnm(points_y),1])
```